Title
The microdosimetric extension in TOPAS: development and comparison with published data

Journal
Physics in Medicine and Biology, 64(14)

ISSN
0031-9155

Authors
Zhu, Hongyu
Chen, Yizheng
Sung, Wonmo
et al.

Publication Date
2019-07-01

DOI
10.1088/1361-6560/ab23a3

Peer reviewed

HHS Public Access

Author manuscript

Phys Med Biol. Author manuscript; available in PMC 2020 July 11.

Published in final edited form as:

Phys Med Biol. ; 64(14): 145004. doi:10.1088/1361-6560/ab23a3.

The microdosimetric extension in TOPAS: Development and comparison with published data

Hongyu Zhu[1,2,3], **Yizheng Chen**[1,2,3], **Wonmo Sung**[1,4], **Aimee L. McNamara**[1,4], **Linh T. Tran**[5], **Lucas N. Burigo**[6], **Anatoly B. Rosenfeld**[5], **Junli Li**[2,3], **Bruce Faddegon**[7], **Jan Schuemann**[1,4], **Harald Paganetti**[1,4]

[1]Department of Radiation Oncology, Massachusetts General Hospital, Boston, MA 02114, USA

[2]Department of Engineering Physics, Tsinghua University, Beijing 100084, People's Republic of China

[3]Key Laboratory of Particle & Radiation Imaging (Tsinghua University), Ministry of Education, Beijing 100084, People's Republic of China

[4]Harvard Medical School, Boston, MA 02114, USA

[5]Centre for Medical Radiation Physics, University of Wollongong, Australia

[6]German Cancer Research Center-DKFZ, Im Neuenheimer Feld 280, D-69120 Heidelberg, Germany

[7]Department of Radiation Oncology, University of California San Francisco, CA 94143, USA

Abstract

Microdosimetric energy depositions have been suggested as a key variable for the modeling of the relative biological effectiveness (RBE) in proton and ion radiation therapy. However, microdosimetry has been underutilized in radiation therapy. Recent advances in detector technology allow the design of new mico- and nano-dosimeters. At the same time Monte Carlo simulations have become more widely used in radiation therapy. In order to address the growing interest in the field, a microdosimetric extension was developed in TOPAS. The extension provides users with the functionality to simulate microdosimetric spectra as well as the contribution of secondary particles to the spectra, calculate microdosimetric parameters, and determine RBE with a biological weighting function approach or with the microdosimetric kinetic model. Simulations were conducted with the extension and the results were compared with published experimental data and other simulation results for three types of microdosimeters, a spherical tissue equivalent proportional counter (TEPC), a cylindrical TEPC and a solid state microdosimeter. The corresponding microdosimetric spectra obtained with TOPAS from the plateau region to the distal tail of the Bragg curve generally show good agreement with the published data.

1. Introduction

High-energy proton and heavy-ion beams are widely used for the treatment of malignant tumors due to the excellent dose localization (Kamada, 2012; Jensen *et al.*, 2011; Schardt *et al.*, 2010; Durante and Loeffler, 2010). Therapeutic high energy proton and heavy-ion beams produce a complex radiation field and the statistical fluctuations of the deposited energy can

be very large on the micrometer scale of human cells (Rossi, 1979). Microdosimetry aims to investigate the transfer of energy from different types of radiation to micro-sized volumes of cellular or sub-cellular scales, using distributions of the lineal energies. Microdosimetric measurements offer a valuable method to characterize the complexities of a radiation field and to assess relative biological effectiveness (RBE) values by applying a biological weighting function approach (Endo *et al.*, 2007; Gerlach *et al.*, 2002; Paganetti *et al.*, 1997; Coutrakon *et al.*, 1997; De Nardo *et al.*, 2004b) or the Microdosimetric Kinetic (MK) model (Tran *et al.*, 2017; Kase *et al.*, 2006) to the measured microdosimetric spectra. Monte Carlo (MC) simulations can be a valuable supplement to experimental microdosimetric measurements to investigate microdosimetric characteristic of different kinds of charged particles and scenarios once they are validated with a set of initial experiments (Chiriotti *et al.*, 2017; Galer *et al.*, 2017; Dewey *et al.*, 2017; Burigo *et al.*, 2015, 2014; Böhlen *et al.*, 2012; Böhlen *et al.*, 2011).

In this work, a microdosimetric extension was developed in TOPAS (TOol for PArticle Simulation) (Perl *et al.*, 2012). TOPAS wraps and extends the MC toolkit Geant4 (Allison *et al.*, 2006; Agostinelli *et al.*, 2003), to provide users with advanced functionality. The lineal energy scorer developed previously (Underwood *et al.*, 2017) was adapted for spherical TEPCs, cylindrical TEPCs and a silicon on insulator (SOI) microdosimeter, and a TOPAS geometry extension of the SOI microdosimeter was developed. To validate the scorer and show the application of the geometry extension, simulations were conducted for these three detectors and compared with experimental results as well as other MC simulation data. In addition, the potential to use microdosimetric simulations for RBE calculations was assessed.

2. Method

2. 1. Basics of microdosimetry and RBE modeling

To assess the radiation damage to cells one needs to understand the patterns of energy deposition within a micrometer sized region, e.g. the cell nucleus. To simulate such small volumes experimentally, tissue equivalent proportional counters (TEPCs) are essential tools. The amount of energy delivered to the TEPC's sensitive volume (SV) by particles traversing the detector fluctuates due to the stochastic nature of particle transport in media (ICRU, 1983). A TEPC measures a probability distribution of lineal energy, $y = \epsilon/\bar{l}$, where ϵ is the energy deposited in the SV by one event and $\bar{l}$ is the mean chord length of the SV.

Microdosimetry provides single-event energy spectra that relate the absorption of ionizing radiation in detectors to that in biological targets (e.g., single cells). One type of microdosimetric spectra that is often used is displaying $yd(y)$ versus $\log(y)$ with:

$$yd(y) = \frac{y^2 f(y)}{\int_0^\infty y f(y) \mathrm{d}y} = \frac{y^2 f(y)}{\overline{y_F}} \quad (1)$$

where $f(y)$, the frequency probability density distribution of lineal energy, is the number of events in the lineal energy interval $\mathrm{d}y$. $f(y)$ is usually characterized by the frequency-mean lineal energy, $\overline{y_F}$, which is defined as:

$$\overline{y_F} = \int_0^\infty y f(y) \mathrm{d}y \tag{2}$$

Another frequently used property is the dose-mean lineal energy, $\overline{y_D}$, which is calculated as:

$$\overline{y_D} = \int_0^\infty y d(y) \mathrm{d}y = \frac{\int_0^\infty y^2 f(y) \mathrm{d}y}{\int_0^\infty y f(y) \mathrm{d}y} = \frac{\int_0^\infty y^2 f(y) \mathrm{d}y}{\overline{y_F}} \tag{3}$$

Here $d(y) = yf(y)/\overline{y_F}$ is introduced as the dose probability density of lineal energy. Further details of the microdosimetry theory can be found elsewhere (ICRU, 1983).

Microdosimetric spectra can be used to characterize a radiation field. Consequently, an RBE can be obtained by combining microdosimetric quantities with biological weighting functions (Paganetti *et al.*, 1997; Coutrakon *et al.*, 1997; Pihet *et al.*, 1990) or the Microdosimetric Kinetic (MK) model (Hawkins, 2003; Kase *et al.*, 2006). The biological weighting function approach is a biophysical model first described by Pihet *et al.* (Pihet *et al.*, 1990) and was applied to predict the biological effectiveness of ionizing radiation (Pan *et al.*, 2015; Gerlach *et al.*, 2002; Paganetti *et al.*, 1997; Coutrakon *et al.*, 1997). With the biological weighting function, $r(y)$, and the dose probability density of lineal energy, $d(y)$, RBE can be estimated according to the relation:

$$RBE = \int r(y) d(y) dy \tag{4}$$

Another microdosimetry based RBE approach is the MK model, a phenomenological model that was first introduced by R. B. Hawkins (Hawkins, 2003) and then modified by Kase, Y et al. (Kase *et al.*, 2006). According to the linear-quadratic (LQ) model, the survival fraction of cells S at the exposure dose D is calculated as:

$$S = \exp\left[-\alpha D - \beta D^2\right] \tag{5}$$

And α could be estimated as:

$$\alpha = \alpha_0 + \frac{\beta}{\rho \pi r_d^2} y^* \tag{6}$$

Here α_0 represents the initial slope of the survival fraction curve in the limit of zero LET, β is a radiation independent parameter, ρ is the assumed density of tissue and r_d is the radius of a sub-cellular domain in the MK model. The saturation-corrected dose-mean lineal energy, y^*, is determined from experimentally measured microdosimetric spectra as:

$$y^* = \frac{y_0^2 \int_0^\infty \left(1 - \exp\left(-y^2/y_0^2\right)\right) f(y) dy}{\overline{y_F}} \tag{7}$$

Here, y_0 is the saturation parameter, which is used to correct the overkilling effect for high LET radiation. And according to the LQ model, the RBE is then calculated using the following relation:

$$RBE = \frac{D_R}{D} = \frac{2\beta D_R}{\sqrt{\alpha^2 - 4\beta \ln(S)} - \alpha} \quad (8)$$

Here, D is the ion dose at a cell survival level S and D_R is the dose of the reference radiation at the same survival fraction.

2.2. TOPAS

TOPAS is a MC simulation toolkit layered on top of Geant4, to make simulations more readily available to both research and clinical medical physicists, as well as to extend its functionality (Perl *et al.*, 2012). Users can control all the TOPAS simulation components including geometry, source, physics, visualization, etc. with a custom-designed parameter control system. The latest distribution of TOPAS is version 3.1.p3, which is based on Geant4 10.03 patch2 and can be downloaded from www.topasmc.org.

2.2.1 The microdosimetric extension—The microdosimetric extension was developed in TOPAS to provide users with advanced functionality in order to apply the microdosimetric formalism described above. A lineal energy scorer that is applicable to three types of microdosimeters (a spherical TEPC, a cylindrical TEPC and a SOI microdosimeter) was developed.

To use the lineal energy scorer, users should first define a detector geometry which is independent from the scorer and add several command lines to provide some basic parameters (shown in Table 1) in the TOPAS parameter file. The users need to specify which type of microdosimeter (*GeometryNumber*) is used in the simulation. The radius (*SensitiveVolumeRadius*) and position of the SV(*TransX/Y/Z*) should be provided to determine the volume for scoring, if the scorer is used for cylindrical TEPC, the half-length (*SensitiveVolumeHalfLength*) of the SV should also be provided. Finally, the tissue equivalent radius (*TissueEquivalentRadius*) should be provided to calculate the mean chord length of the SV with the Cauchy formula, $\bar{l} = 4V/S$, where V is the volume of the SV and S is the surface area of the SV (Cauchy, 1908). For a spherical TEPC and a cylindrical TEPC, $\bar{l}$ is calculated as $\bar{l} = 4 \cdot TissueEquivalentRadius/3$. For the special case of a SOI microdosimeter described below, a mean path length (*MeanPathLength*) rather than mean chord length was used to convert the energy deposition into lineal energy (Bolst *et al.*, 2017b). With these parameters, the scorer records every interaction, with an energy deposition greater than zero, of both the primary and secondary particles in the material of the SV of the detector. The total energy deposition, ϵ, for each primary event is then divided by the mean chord length (or mean path length) of the SV and converted to lineal energy, y. At the end of the simulation, the recorded lineal energies are binned to get the frequency probability density distribution of lineal energy as:

$$f(y_i) = \frac{n(y_i)}{\sum n(y_i) \cdot \Delta y_i} \quad (9)$$

Here, $n(y_i)$ is the number of recorded lineal energy hits in the i-th bin, $\Sigma n(y_i)$ is the total number of recorded lineal energy hits, and Δy_i is the width of i-th bin (e.g. 0–10 can be uniformly divided into 10 bins with a bin width of 1). If the lineal energy of one event is scored in the i-th bin of the total microdosimetric spectrum, then the total energy deposition (ϵ_{total}) and the secondary particle energy deposition ($\epsilon_{secondary}$) will be scored and accumulated in the i-th bin of the total energy deposition histogram and the secondaries energy deposition histogram, respectively. In the end, the secondary particle contribution is calculated by the ratio of energy deposition of the secondary particles to the total energy deposition in each bin. Other microdosimetric quantities can then be calculated as described in 2.1.

The frequency probability density distribution could be updated every time a new event is scored. At the end of simulation, the statistical uncertainty for each bin of $f(y)$ is calculated with Eq.(10) (Knuth, 1997).

$$\sigma_{f(y_i)} = \sqrt{\left(N \sum_{1 \le k \le N} f(y_i)_k{}^2 - \left(\sum_{1 \le k \le N} f(y_i)_k\right)^2\right) N(N-1)} \quad (10)$$

Here, $f(y_i)_k$ is the value of i-th bin of the frequency probability density distribution after scoring k events, and N is the total number of scored events. The statistic error of other quantities can be calculated using error propagation once $\sigma_{f(y_i)}$ is obtained. However, for sufficient statistical robustness, one may need to simulate millions of primary events in a microdosimetric simulation and updating $f(y)$ each time a new event is scored can be very time consuming. Therefore, the user has to define if statistical information is wanted by setting the optional boolean parameter *GetStatisticInformation* to true. In addition, users can specify how many times (*SpectrumUpdateTimes*) they want to update $f(y)$ to calculate $\sigma_{f(y_i)}$, e.g. if the value of *SpectrumUpdateTimes* is set as 100/1000/10000 for 10^8 primary histories, the $f(y)$ and the statistic information are updated every $10^6/10^5/10^4$ histories are finished. The calculated statistic uncertainties will be smaller if *SpectrumUpdateTimes* has a smaller value, since more events are simulated before updating $f(y)$.

The scorer offers some other optional parameters. The upper and lower limit to score lineal energy are by default set as 0 and 10,000 keV/μm, respectively, and can be adjusted by the user. Explicit calculation of $\overline{y_F}$, $\overline{y_D}$ and contributions of secondary particles to the microdosimetric spectrum can optionally be requested. In addition, users can choose which method to use to calculate RBE and set the parameters in the MK model or provide their own biological weighting function data. In addition to all the mandatory and optional parameters offered in the microdosimetric scorer, TOPAS allows users to combine different filters with the scorer to score only primary or secondary particles, particles with a certain atomic mass or number, etc. (cf.topas.readthedocs.org website). Figure 1 shows a snippet of a parameter file to illustrate how to invoke the lineal energy scorer and set the necessary

parameters in a TOPAS simulation. The definitions of geometry, source, physics, and other parameters required for the TOPAS simulation (cf.topas.readthedocs.org website and in Perl *et al.*(Perl *et al.*, 2012)) are not shown for simplicity.

The output files of the lineal energy scorer include a n-tuple record of lineal energy in ASCII, binary or ROOT format and a microdosimetric spectrum file, which contains the value and statistic information of y, $f(y)$, $yf(y)$, $d(y)$, and $yd(y)$ binned in log scale, in ASCII format.

2.2.2 Microdosimeter models in TOPAS

Spherical TEPC: In the past decade, many microdosimetric measurements were performed with the commercially available Far West Technologies LET-1/2 spherical TEPC (Kase *et al.*, 2011; Martino *et al.*, 2010; Kase *et al.*, 2006; Borak *et al.*, 2004; Nakane and Sakamoto, 2001; Kellerer, 1981). The spherical TEPC consists of a tissue equivalent (TE) sphere made of A-150 plastic (H (10.1%), C (77.6%), N (3.5%), O (5.2%), F (1.7%) and Ca (1.9%)), a collecting wire of stainless steel and an outer aluminum shell. The inner cavity of A-150 plastic sphere has a diameter of 12.7 mm and is filled with TE gas and functions as the sensitive volume of the detector. The wall thickness of the A-150 plastic shell is 1.27 mm. The aluminum shell is used as a vacuum tight container outside the TE plastic sphere with a thickness of 0.18 mm and 20 mm outer diameter. For simulation purposes, the spherical TEPC model can be simplified as four concentric spheres, as shown in Figure 2. The central anode wire can be ignored because of the low probability of particles interacting with this wire (Burigo *et al.*, 2013).

Martino *et al.* used the spherical TEPC to measure microdosimetric spectra of a 300 MeV/u carbon ion beam at GSI (Gesellschaft für Schwerionenforschung, Darmstadt, Germany) (Martino *et al.*, 2010). In the experiment, the TEPC was placed in a 300 × 300 × 300 mm^3 water phantom at the depth of 25 mm, 152 mm and 250 mm corresponding to the plateau, the Bragg peak position and the tail region respectively. The TEPC was filled with propane based TE gas (C_3H_8 (55%), CO_2 (39.6%) and N_2 (5.4%)) and operated with a gas pressure corresponding to a sphere of tissue of 2.7 μm in diameter.

Burigo *et al.* reproduced this experiment with the Geant4-based Monte Carlo model for Heavy Ion Therapy (MCHIT) (Pshenichnov *et al.*, 2010; Pshenichnov *et al.*, 2008; Pshenichnov *et al.*, 2007; Pshenichnov *et al.*, 2006), and compared the simulation results with the measured spectra (Burigo *et al.*, 2014, 2013). The source was set as a 300 MeV/u carbon ion beam with a size of 3 mm FWHM, an angular distribution with the Gaussian profile of 1 mrad FWHM, and a Gaussian energy spread of 0.2% FWHM. The beam-line elements and PMMA wall of the water phantom in the experiment were estimated as an equivalent water thickness of 25.1 mm (Burigo *et al.*, 2013). This thickness was applied to the detector depth in the simulation, and the simulation was performed with a wall-less water phantom of 300×300×300 mm^3. Burigo *et al.* found that in order to reproduce the peak in the $yd(y)$ spectrum for the TEPC positioned in the vicinity of the Bragg peak on the beam axis with MCHIT, a slightly shift to a deeper position of the detector is required. This shift may be attributed to uncertainties in the positioning of the TEPC during the experiment, the beam energy as well as the water equivalent thickness in front of the water

phantom. Potential inaccuracies of the electromagnetic physics models in Geant4 might also have some contribution (Burigo *et al.*, 2013). Therefore, considering the water equivalent thickness in front of the phantom and the depth shift, the simulated detector was placed on the beam axis at depths of 52.1 mm, 179.1 mm and 277.1 mm in the water phantom, i.e. the detector depth in the wall-less water phantom in MCHIT simulations equals the detector depth in the water phantom in the experiment (25/152/250 mm) plus the water equivalent thickness in front of the phantom (25.1 mm) and the depth shift (2 mm). Burigo *et al.* considered several predefined physics lists of Geant4 to describe the electromagnetic processes and two different customized physics lists for the modeling of nuclear fragmentation reactions, including the Light Ion Binary Cascade (G4BIC) model and the Quantum Molecular Dynamics (G4QMD). In addition, to compare the microdosimetric spectra simulated by MCHIT with those measured in the experiment, two steps of normalization were performed by Burigo *et al* (Burigo *et al.*, 2013). First, the lineal energy probability density, $f(y)$ of the experimental spectra was scaled by a factor of 0.844 as a correction of the experimental data because the integral of $f(y)$ in the plateau region was more than 1 (Burigo *et al.*, 2013). Second, the microdosimetric spectra were normalized to the ion fluence as:

$$yd(y)/ion = \frac{y^2 f(y)}{\bar{y}_F} \cdot \int_0^\infty f(y)\mathrm{d}y \tag{11}$$

where $f(y)$ was normalized to per primary particle.

In order to evaluate the implementation of the spherical TEPC in TOPAS, the experimental settings from Martino *et al* (Martino *et al.*, 2010) and simulation settings from Burigo *et al* (Burigo *et al.*, 2013) were adopted. The geometry of the spherical TEPC as well as the setup geometry defined in the TOPAS simulation are shown in Figure 2. The default TOPAS physics list was applied, which contains the hadronic physics models of Light Ion Binary Cascade (G4BIC), G4ExcitationHandler and Fermi break-up model. The Geant4 “Standard Electromagnetic Physics Option 3” model was used for the electromagnetic processes. Range cuts, i.e. a particle production threshold to stop producing secondary particles unable to travel at least the given extrapolated range, for electrons in water, A-150 plastic and TE gas were set as 0.1 mm, 0.01 mm and 9 mm, respectively, and the corresponding energy thresholds are 85.0, 17.6 and 0.99 keV. Considering that the experimental microdosimetric spectra were reported only above 0.3–0.5 keV/μm, only y values larger than 0.3 keV/μm were scored. The TEPC was placed on the beam axis with 52.1 mm, 179.1 mm and 277.1 mm depths in the water phantom and the microdosimetric spectra obtained with TOPAS were normalized according to Eq.(11). 10^7 primary particles were simulated for the depth of 52.1 and 179.1 mm and 10^8 primary particles were simulated for the depth of 277.1 mm.

Cylindrical TEPC: Although the Far West Technologies LET-1/2 spherical TEPC is widely used, it’s relatively large size limits its application when measuring in the Bragg peak region which is only a few millimeters wide (Chiriotti *et al.*, 2017). In addition, for radiation fields with a high fluence rate signals of multiple tracks can overlap (De Nardo *et al.*, 2004a). To cope with the high beam intensity of therapeutic ion beams, a cylindrical mini-TEPC with a SV size less than 1 mm was developed at LNL-INFN (Moro *et al.*, 2006; De Nardo *et al.*,

2004a). Due to its small external size, the mini-TEPC can collect data in the Bragg peak region with high accuracy. The cylindrical mini-TEPC (De Nardo *et al.*, 2004a) has a cylindrical SV of 0.9 mm in diameter and height and is axially defined by two Rexolite ($(C_8H_8)_n$) insulator disks. The gas cavity is filled with TE gas and surrounded by a 0.35 mm-thick A-150-cathode wall, a 0.35 mm thick Rexolite® insulator and a 0.2 mm thick aluminum sleeve for a total external diameter of 2.7 mm (Rollet *et al.*, 2010).

Microdosimetric measurements with the cylindrical TEPC were performed in a water phantom at the Italian National Centre for Oncological Hadrontherapy (CNAO) with a mono-energetic carbon ion beam of 195.2 MeV/u modulated by using two ripple filters of 2 mm peak width made of PMMA. The resulting 12C beam had an average energy of 189.5 MeV/u and a FWHM of 0.3 MeV/u at the isocenter and irradiated a field of 30 × 30 mm^2 with 225 equally spaced beam spots (Colautti *et al.*, 2017). The SV was filled with C_3H_8 gas corresponding to an SV size of 1 μm of C_3H_8-TE gas at a density of 1 g/cm^3. Furthermore, FLUKA simulations were performed to compare experimental carbon microdosimetric data measured with the mini-TEPC with simulated microdosimetry spectra (Chiriotti *et al.*, 2017).

TOPAS simulations of the cylindrical mini-TEPC were performed following the experimental setup (Figure 3). The default physics list was used in the TOPAS simulation, and following the FLUKA simulations (Chiriotti *et al.*, 2017), the A-150 plastic was divided into a 3 μm thick inner layer that is adjacent to the gas cavity and a 347 μm thick outer layer to speed up the simulation without affecting the accuracy of the results. In the SV and in the innermost thin ring of 3 μm of A-150 plastic, the electron range cut was set as 0.001 mm. In all the other layers, the electron range cut was set as 0.01 mm. Experiment and simulation results were compared for both depth dose distributions and microdosimetric spectra. For the depth dose distribution, 10^6 primary particles were simulated, and the energy depositions were scored in a series of 2.5 mm radius and 1 mm thickness cylindrical volumes, which is the same size as the Markus chamber used in the experiment. For the microdosimetric spectra simulation, 10^7 primary particles were simulated at the plateau region and the Bragg peak position, and 10^8 primary particles were simulated at the distal edge and the distal tail of the Bragg peak.

Silicon on insulator (SOI) microdosimeter: The high voltage bias and gas supply requirements of the TEPC make it less ideal for routine QA in clinical environments. As a solution to this problem, SOI microdosimeters (Bradley *et al.*, 2001) were designed at the Centre for Medical Radiation Physics (CMRP), University of Wollongong, Australia. A SOI microdosimeter is based on an array of micrometer sized SVs mimicking the dimension of cells. Recently, the CMRP has developed SOI microdosimeters consisting of well-defined, micrometer-sized 3D sensitive volumes known as “bridge” microdosimeters (Tran *et al.*, 2015). These detectors contain a grid of SVs (59 rows and 72 columns) placed on top of a 300 μm-thick supporting Si substrate with an upper insulation SiO_2 layer of width 1 μm. Each SV is a 30×30×10 $μm^3$ block of Si connected to adjacent SVs by a 20×15×10 $μm^3$ Si bridging volume. A 1.7 μm-thick SiO_2 layer covers the entire upper surface of the SVs and bridging volumes. On top of the SVs, there is a 4×4×1.7 $μm^3$ aluminum layer in the center

of the SiO_2. Furthermore, there is a 10.5×10.5×1.43 μm^3 SiO_2 layer on the top of SiO_2/Al above the sensitive volume (see Figure 4).

This device was used for microdosimetric measurements at the Massachusetts General Hospital (MGH) Francis H. Burr Proton Beamy Therapy Center (Tran *et al.*, 2017). In the experiment, the proton energy was 131 MeV with a Gaussian energy spread σ of 0.86% (2.65 MeV FWHM), the pencil beam has a σ of 11 mm (FWHM = 2.3548 × σ = 25.9 mm) in air at isocenter, and a range of the distal 90% of the depth-dose, R_{90}, of 124.6 mm was used for measuring lineal energy distributions.

These experiments were simulated using TOPAS. To simplify the parameter list needed to invoke the SOI microdosimeter in TOPAS, a geometry extension for the SOI microdosimeter was created according to the description above and shown in Figure 4. Users only need to add a command line as “s:Ge/MyMicrodosimeter/Type=“TsSOIMicrodosimeter”“ to invoke the geometry extension. The default physics list was used in the simulations. The maximum step size in a region of 150 μm surrounding the microdosimeter was set to 1 μm and the electron production cut in range was set to 1 μm in a region of 2 mm surrounding the microdosimeter.

10^6 primary particles were simulated to obtain the depth dose distributions in a water phantom, the does distributions were scored along the beam axis in a cylinder of 2.5 cm diameter, the size of the Zebra (IBA Dosimetry, Germany) multilayer ionization chamber used in the experiment. For microdosimetric spectra simulations, considering that the detection threshold of the detector is 0.3–0.4 keV/μm and that the experimental spectra start from ~0.5 keV/μm, the lower threshold to score linear energy was set to 0.5 keV/μm in the TOPAS simulation. The energy deposition in the SOI detector was scored by row, which means 72 SVs in one row were regarded as a single channel. Each time a particle track traverses a SV, the energy it deposited was scored in the channel the SV was in. If a track traverses multiple SVs, the energy deposited in each SV was summed for the respective channel. The final energy depositions in each channel for each event were scored and scaled by the tissue equivalent conversion factor (F = 0.58), which is used to convert the energy deposition in the SV of the SOI microdosimeter to the energy deposition in a tissue equivalent spherical SV, to get the equivalent energy deposition in tissue and then divided by the mean path length to convert energy deposition into lineal energy. The mean path length, which was introduced by Bolst *et al.* (Bolst *et al.*, 2017a) and used here differs from the mean chord length given by the Cauchy formula, which gives the mean chord length for randomly distributed chords in a volume and only applies to isotropic radiation fields. In this work, the mean path length was adopted as 10 μm representing the thickness of the silicon layer in the SV (Bolst *et al.*, 2017b). 10^7 primary particles were simulated before the Bragg peak position, and 10^8 primary particles were simulated at the distal edge and the distal tail of the Bragg peak. The microdosimetric spectra obtained with TOPAS were normalized to unity to compare with the spectra obtained experimentally.

3. Result and Discussion

The following sections show comparisons between results simulated with the microdosimetric extension of TOPAS and published data using either Monte Carlo simulations with other codes or experiments.

3.1. Spherical TEPC

The microdosimetric spectra corresponding to the plateau, Bragg peak and tail regions along the beam axis obtained in the experiment and simulated with MCHIT with the G4BIC model and TOPAS are compared in Figure 5. The contributions of secondary particles are presented in Figure 6. The spectra at different depth obtained with TOPAS are generally in good agreement with the microdosimetric spectra simulated with MCHIT, which is expected since both codes are based on Geant4, albeit using different versions of the code.

At the plateau region (Figure 5 (a)), the main peak of the microdosimetric spectrum is associated with the primary beam particles and is well reproduced by the simulated spectra. However, the simulated results are lower than the experimental spectra in the range of $20 < y < 200$ keV/μm. This might be a slight signal pile-up effect in the experiment, this was validated by adding a pile-up probability in the simulation, i.e., the energy deposition of each event might be held and add to the energy deposition of the next event with a probability of P_{pu}, the resulting microdosimetric spectra were also shown in Figure 5. As seen, the agreement between the experimental and simulated spectra was restored after accounting for the pile-up effect with a pile up probability of 2%. The discrepancy at the lineal region of 20–200 keV/μm can, in part, also be attributed to the energy threshold for production and transport of δ-electrons used in the simulation. In the MC simulation, the interface of TE wall with TE gas imposes a challenge for the condensed history MC. The cut in range applied in the simulation corresponds to a production threshold of 17.6 keV in the TE wall and 0.99 keV in the SV (minimum energy of the electromagnetic models in Standard Electromagnetic Physics Option 3). In close proximity to the SV for the detector placed at the plateau region, some secondary electrons could have enough energy to enter the SV, but they might be truncated due to their short projected range in the TE wall below the production range. This may result in an underestimation of the secondary electrons entering the SV and cause the reduced energy deposition there. Conversely, secondary electrons in the SV with energy as low as 990 eV have relatively large range compared to the SV and can escape the volume. Differently, at the Bragg peak position, since although more secondary electrons are produced, they are generally less energetic compared to those at the plateau region what changes the impact of the energy production threshold.

In the Bragg peak position (Figure 5 (b)), the simulated spectra are lower than the experimental data for $y<70$ keV/μm. As shown in Figure 6 and according to Burigo et al. (Burigo *et al.*, 2013) the peak is caused by relatively heavy projectile fragments (boron, beryllium lithium and helium nuclei) propagating with velocities close to the velocity of the primary particles. The underestimation at the low lineal energy region indicates that secondary fragments are underestimated by the nuclear fragmentation models used in the simulation.

As for the tail region (Figure 5 (c)), the distribution of the microdosimetric spectrum is mostly including neutrons. Considering that it is a fragmentation tail, the discrepancy could have the same explanation as in Figure 5 (b). A contributing factor may be that the fluence of neutrons is underestimated by the physics model.

The frequency mean lineal energy, $\overline{y_F}$, dose mean lineal energy $\overline{y_D}$, obtained in experiment and simulation, and the probability to deposit energy in the TEPC per beam particle at various depths, P_{TEPC}, obtained in simulation are shown in Table 2. Considering that the experimental data reported are only in the range of 0.3–1000 keV/μm, the microdosimetry parameters obtained from TOPAS and MCHIT simulations were computed only in the lineal energy interval of available experimental data. The small difference between TOPAS 3.1.3 and MCHIT might result from the modification of the physical models in the underlying Geant4 (versions 10.3.p2 and 9.4, respectively). The results obtained with a custom built TOPAS version based on TOPAS 3.1.3 compiled with Geant4.10.4.p2 are also presented in table 2 to demonstrate the model dependency, since the only difference between the two TOPAS versions is the Geant4 software version.

3.2. Cylindrical TEPC

The comparison of depth dose distributions obtained experimentally and simulated with FLUKA and TOPAS are shown in Figure 7. When the energy of the primary carbon ions was set to 189.5 ± 0.3 MeV/u in the TOPAS simulation, the Bragg peak position was shallower and the relative dose was lower at the plateau region compared to the FLUKA simulations and the experiment. The discrepancy might be attributed to the fact that the FLUKA simulations included a detailed geometry of the beamline to transport primary carbon ions and secondary particles and record a phase space (PS) file for further simulation (Chiriotti *et al.*, 2017) while in the TOPAS simulation the source was simplified as a mono-energetic beam with a rectangle shape and flat position distribution due to the lack of information about the beamline geometry. In addition, TOPAS rely on a different stopping power formalism, TOPAS (Geant4) uses revised ICRU 73 stopping power tables and FLUKA uses the Bethe formula with shell, Barkas and Bloch corrections to calculate stopping powers for high energy (Paul and Sánchez-Parcerisa, 2013). The energy of primary carbon ions was adjusted to 192 ± 1.15 MeV/u for the TOPAS simulation to force an agreement in the peak position of the depth dose with the experiment and FLUKA results.

In the plateau region, several positions were considered because at 40.2 mm and 60.2 mm there are only FLUKA simulated data available for comparison and at 61.3 mm there is only experimental data available for comparison. The simulation results obtained with TOPAS agree reasonably well with FLUKA in the plateau region (Figure 8 (a)), however, the position of the microdosimetric spectrum does not agree with the experimental results. It is possible that this is caused by secondary lower LET contamination (neutrons) of the experimental beam in the entrance of the Bragg curve and underestimation of fragments by the Geant4 physics model used.

Comparing spectra at other positions (Figure 8 (b)–(d)), it was found that the microdosimetric spectra obtained with TOPAS tend to represent the spectra in the peak

region very well. Considering that the positioning uncertainty of the detector in the experiment is bigger than 0.6 mm (Colautti *et al.*, 2017) and that the mini-TEPC was enclosed with a PMMA structure in the experiment for which details were not provided in the reference (Colautti *et al.*, 2017; Chiriotti *et al.*, 2017), the simulated detector was slightly shifted by between 0.5 and 2 mm for each independent spectrum measurement in the water phantom to get a better match of the microdosimetric spectra. After this shift, the microdosimetric spectra obtained with TOPAS are generally in good agreement with the experimental spectra. The remaining discrepancy between spectra obtained with FLUKA and TOPAS might be attributed to the difference in physics models and nuclear interaction cross section data between these two codes.

3.3. SOI microdosimeter

Depth dose distributions obtained experimentally with a multilayer ionization chamber and simulated with TOPAS are compared in Figure 9. A slight difference (0.9 mm) in the Bragg peak position is acceptable considering the positioning uncertainty in the experiment is ± 1 mm (Tran *et al.*, 2017).

The microdosimetric spectra obtained experimentally and simulated with TOPAS are shown in Figure 10. The comparison is performed at different depths from the plateau region to the distal tail of the Bragg peak. The area under the microdosimetry spectrum ($\Sigma yd(y)\Delta y$) was normalized to unity to compare with the experimental data. Although the range of the simulated microdosimetry spectra is within 100 keV/μm, some rare high energy deposition events could contribute counts in the area >100 keV/μm. This contribution is invisible on the $y - yd(y)$ spectrum but can have a big impact on the area of the microdosimetric spectrum. Therefore, only the area within 100 keV/μm was used for the normalization.

The simulated spectra and experimental spectra are generally in good agreement in the plateau region (22 mm) and the distal part of the Bragg peak (126 and 129 mm). However, the experimental spectra are higher than the simulated spectra at the low lineal energy region, this might be caused by the photons and neutrons in the experiment after the long-time irradiation. Besides, the detector was gradually moved to a deeper depth in the experiment, this makes the discrepancy increases with the detector depth because the increase of total irradiation time results in a larger contribution of photons and neutrons. The spectrum obtained with TOPAS at 125 mm agrees better with the experimental spectrum at 126 mm. This 1 mm shift is within the experimental uncertainty. At 110 and 122 mm, the discrepancy between the simulated and measured spectra is significant. In the region of the Bragg peak position, the microdosimetric spectrum is very sensitive to the detector positioning. The inconsistency of the microdosimetric spectra at 110 and 122 mm might be attributed to detector positioning considering that the spectra agree well at the other three positions obtained in separate experimental runs. Besides, the water phantom wall and all covered materials in front of the detector were taken into account for the water equivalent thickness and applied to the depth of the SOI microdosimeter in the experiment. The uncertainties in the estimate of water equivalent thickness may contribute to the difference between simulation and experimental results.

3.4. RBE calculated with biological weighting function and the MK model

The RBE based on the microdosimetric spectra obtained with TOPAS for the SOI detector was calculated with the biological weighting function approach and the MK model. The results are shown in Figure 11. The biological weighting function $r(y)$ for the biological end point of early intestinal tolerance assessed by crypt regeneration in mice (Loncol *et al.*, 1994) was used to obtain RBE with the biological weighting function approach. For the MK model, parameters for 10% cell survival relative to the reference radiation (200 kVp X-rays) for HSG cells were used to calculate RBE_{10} values. The 10% survival dose of 200 kVp X-rays for HSG cells is 5.14 Gy and the adopted parameters for Eq.(6)–(7) are , $\alpha_0 = 0.13$ Gy^{-1}, $\beta = 0.05$ Gy^{-2}, $\rho = 1$ $g{\cdot}cm^{-3}$, $r_d = 0.42$ μm, and y_0 is fixed to the value of 150 keV/μm (Kase *et al.*, 2006). The in RBE values calculated from microdosimetric spectra will vary over the data of biological weighting function (Paganetti *et al.*, 1997) and parameters adopted in the MK model. RBE values were calculated with a phenomenological RBE model, which is based on the linear quadratic model and was derived from a nonlinear regression fit to experimental data, with Eq.(12) (McNamara *et al.*, 2015) to serve as reference RBE values.

$$RBE\left[D_p, (\alpha/\beta)_x, LET_D\right] = \frac{1}{2D_p} \left(\sqrt{\left(\frac{\alpha}{\beta}\right)_x^2 + 4D_p\left(\frac{\alpha}{\beta}\right)_x\left(p_0 + \frac{p_1}{(\alpha/\beta)_x}LET_D\right) + 4{D_p}^2\left(p_2 + p_3\sqrt{\left(\frac{\alpha}{\beta}\right)_x}LET_D\right)^2} - \left(\frac{\alpha}{\beta}\right)_x\right) \quad (12)$$

Here, p_0 =0.99064, p_1 =0.35605, p_2=1.1012, p_3=−0.0038703,D_p is the dose, LET_D is the dose average linear energy transfer (LET) and $(\alpha/\beta)_x$ is the ratio of the linear-quadratic model parameters for the reference radiation. In the calculation, *Dp* and *LETD* were scored within the SV of SOI detector, and $(\alpha/\beta)_x$ was adopted as $\alpha_x = 0.19$ Gy^{-1} and $\beta_x = 0.05$ Gy^{-2} for a 200 kVp × ray (Kase *et al.*, 2006).

The discrepancy between the RBE predictions is not surprising given the fundamentally different approaches and the fact that model parameters were based on separate sets of empirical input data.

4. Conclusion

An extension to TOPAS that allow users to simulate microdosimetric quantities such as the lineal energy was developed. The extension is currently applicable to three types of microdosimetric detectors, a spherical TEPC, a cylindrical TEPC and a SOI “bridge” microdosimeter with all geometries becoming available in the next TOPAS release. Based on these examples further detectors can be implemented. In addition, the extension includes two models to calculate RBE based on microdosimetric quantities, a biological weighting function approach and the MK model.

Microdosimetric spectra and parameters for the three detector types were obtained with the extension, and results were compared with experimental and other simulation results from the literature. Different range cuts, step length limits, scoring limits, and normalization

methods were adopted for each type of detector, to match the experimental conditions or the parameters used by the other simulation codes. The published data did not include all the necessary information to reconstruct the beam delivery and experimental procedures, except for the case with the SOI microdosimeter with experiments performed at our institution. Given the sensitivity of microdosimetric spectra to beam characteristics and detector positioning, the results obtained with TOPAS is generally in good agreement with the experimental, MCHIT, and FLUKA results. The microdosimetric extension is generic and in combination with TOPAS functionality, e.g. filtered scoring and the extension system where users can add their own geometric components or scorers.

Acknowledgments

Hongyu Zhu was sponsored by China Scholarship Council for one-year study at the Massachusetts General Hospital. This work was supported by the National Cancer Institute under R01 CA187003 (TOPAS - nBio, a Monte Carlo tool for radiation biology research) and U24 CA215123 (The TOPAS Tool for Particle Simulation, a Monte Carlo Simulation Tool for Physics, Biology and Clinical Research).

References

Agostinelli S, Allison J, Amako K a, Apostolakis J, Araujo H, Arce P, Asai M, Axen D, Banerjee S and Barrand G 2003 GEANT4—a simulation toolkit Nuclear instruments and methods in physics research section A: Accelerators, Spectrometers, Detectors and Associated Equipment 506 250–303

Allison J, Amako K, Apostolakis J, Araujo H, Dubois PA, Asai M, Barrand G, Capra R, Chauvie S and Chytracek R 2006 Geant4 developments and applications IEEE Transactions on nuclear science 53 270–8

Böhlen TT, Dosanjh M, Ferrari A and Gudowska I 2012 Simulations of microdosimetric quantities with the Monte Carlo code FLUKA for carbon ions at therapeutic energies International journal of radiation biology 88 176–82 [PubMed: 21913815]

Böhlen TT, Dosanjh M, Ferrari A, Gudowska I and Mairani A 2011 FLUKA simulations of the response of tissue-equivalent proportional counters to ion beams for applications in hadron therapy and space Physics in Medicine & Biology 56 6545 [PubMed: 21937771]

Bolst D, Guatelli S, Tran LT, Chartier L, Lerch ML, Matsufuji N and Rosenfeld AB 2017a Correction factors to convert microdosimetry measurements in silicon to tissue in 12C ion therapy Physics in Medicine & Biology 62 2055 [PubMed: 28151733]

Bolst D, Tran LT, Chartier L, Prokopovich DA, Pogossov A, Guatelli S, Reinhard MI, Petasecca M, Lerch ML and Matsufuji N 2017b RBE study using solid state microdosimetry in heavy ion therapy Radiation Measurements 106 512–8

Borak TB, Doke T, Fuse T, Guetersloh S, Heilbronn L, Hara K, Moyers M, Suzuki S, Taddei P and Terasawa K 2004 Comparisons of LET distributions for protons with energies between 50 and 200 MeV determined using a spherical tissue-equivalent proportional counter (TEPC) and a position-sensitive silicon spectrometer (RRMD-III) Radiation Research 162 687–92 [PubMed: 15548122]

Bradley P, Rosenfeld A and Zaider M 2001 Solid state microdosimetry Nuclear Instruments and Methods in Physics Research Section B: Beam Interactions with Materials and Atoms 184 135–57 [PubMed: 11863030]

Burigo L, Pshenichnov I, Mishustin I and Bleicher M 2013 Microdosimetry of radiation field from a therapeutic 12C beam in water: A study with Geant4 toolkit Nuclear Instruments and Methods in Physics Research Section B: Beam Interactions with Materials and Atoms 310 37–53

Burigo L, Pshenichnov I, Mishustin I and Bleicher M 2014 Microdosimetry spectra and RBE of 1H, 4He, 7Li and 12C nuclei in water studied with Geant4 Nuclear Instruments and Methods in Physics Research Section B: Beam Interactions with Materials and Atoms 320 89–99

Burigo L, Pshenichnov I, Mishustin I and Bleicher M 2015 Comparative study of dose distributions and cell survival fractions for 1H, 4He, 12C and 16O beams using Geant4 and Microdosimetric Kinetic model Physics in Medicine & Biology 60 3313 [PubMed: 25825827]

Cauchy A. 1908; Memoire sur la rectification des courbes et la quadrature des sourface courbe. Oeuvres Completes. 2

Chiriotti S, Conte V, Colautti P, Selva A and Mairani A 2017 Microdosimetric Simulations Of Carbon Ions Using The Monte Carlo Code FLUKA Radiation protection dosimetry 1–5

Colautti P, Conte V, Selva A, Chiriotti S, Pola A, Bortot D, Fazzi A, Agosteo S and Ciocca M 2017 Microdosimetric Study at the CNAO Active-Scanning Carbon-Ion Beam Radiation protection dosimetry 1–5

Coutrakon G, Cortese J, Ghebremedhin A, Hubbard J, Johanning J, Koss P, Maudsley G, Slater C, Zuccarelli C and Robertson J 1997 Microdosimetry spectra of the Loma Linda proton beam and relative biological effectiveness comparisons Medical physics 24 1499–506 [PubMed: 9304579]

De Nardo L, Cesari V, Donà G, Magrin G, Colautti P, Conte V and Tornielli G 2004a Mini-TEPCs for radiation therapy Radiation protection dosimetry 108 345–52 [PubMed: 15103064]

De Nardo L, Moro D, Colautti P, Conte V, Tornielli G and Cuttone G 2004b Microdosimetric investigation at the therapeutic proton beam facility of CATANA Radiation protection dosimetry 110 681–6 [PubMed: 15353730]

Dewey S, Burigo L, Pshenichnov I, Mishustin I and Bleicher M 2017 Lateral variations of radiobiological properties of therapeutic fields of (1)H, (4)He, (12)C and (16)O ions studied with Geant4 and microdosimetric kinetic model Phys Med Biol 62 5884–907 [PubMed: 28557800]

Durante M and Loeffler JS 2010 Charged particles in radiation oncology Nature reviews Clinical oncology 7 37

Endo S, Takada M, Onizuka Y, Tanaka K, Maeda N, Ishikawa M, Miyahara N, Hayabuchi N, Shizuma K and Hoshi M 2007 Microdosimetric evaluation of secondary particles in a phantom produced by carbon 290 MeV/nucleon ions at HIMAC Journal of radiation research 48 397–406 [PubMed: 17690533]

Galer S, Shipley DR, Palmans H, Kirkby KJ and Nisbet A 2017 Monte Carlo simulation of a TEPC for microdosimetry of carbon ions Radiation Physics and Chemistry 140 412–8

Gerlach R, Roos H and M. Kellerer A2002 Heavy ion RBE and microdosimetric spectra Radiation protection dosimetry 99 413–8 [PubMed: 12194343]

Hawkins RB 2003 A microdosimetric-kinetic model for the effect of non-Poisson distribution of lethal lesions on the variation of RBE with LET Radiation research 160 61–9 [PubMed: 12816524]

ICRU. 1983; Microdosimetry. ICRU Report. 36

Jensen A, Münter M and Debus J 2011 Review of clinical experience with ion beam radiotherapy The British journal of radiology 84 S35–S47 [PubMed: 21427183]

Kamada T 2012 Clinical evidence of particle beam therapy (carbon) International journal of clinical oncology 17 85–8 [PubMed: 22426888]

Kase Y, Himukai T, Nagano A, Tameshige Y, Minohara S, Matsufuji N, Mizoe J, Fossati P, Hasegawa A and Kanai T 2011 Preliminary calculation of RBE-weighted dose distribution for cerebral radionecrosis in carbon-ion treatment planning Journal of radiation research 52 789–96 [PubMed: 21921434]

Kase Y, Kanai T, Matsumoto Y, Furusawa Y, Okamoto H, Asaba T, Sakama M and Shinoda H 2006 Microdosimetric measurements and estimation of human cell survival for heavy-ion beams Radiat Res 166 629–38 [PubMed: 17007551]

Kase Y, Yamashita W, Matsufuji N, Takada K, Sakae T, Furusawa Y, Yamashita H and Murayama S 2013 Microdosimetric calculation of relative biological effectiveness for design of therapeutic proton beams J Radiat Res 54 485–93 [PubMed: 23179376]

Kellerer AM 1981 Criteria for the equivalence of spherical and cylindrical proportional counters in microdosimetry Radiation research 86 277–86

Knuth DE 1997 The art of computer programming, volume 2 (3rd ed.): seminumerical algorithms

Loncol T, Cosgrove V, Denis J, Gueulette J, Mazal A, Menzel H, Pihet P and Sabattier R 1994 Radiobiological effectiveness of radiation beams with broad LET spectra: microdosimetric analysis using biological weighting functions Radiation Protection Dosimetry 52 347–52

Martino G, Durante M and Schardt D 2010 Microdosimetry measurements characterizing the radiation fields of 300 MeV/u 12C and 185 MeV/u 7Li pencil beams stopping in water Physics in Medicine & Biology 55 3441 [PubMed: 20508316]

McNamara AL, Schuemann J and Paganetti H 2015 A phenomenological relative biological effectiveness (RBE) model for proton therapy based on all published in vitro cell survival data Phys Med Biol 60 8399–416 [PubMed: 26459756]

Moro D, Colautti P, Gualdrini G, Masi M, Conte V, De Nardo L and Tornielli G 2006 Two miniaturised TEPCs in a single detector for BNCT microdosimetry Radiation protection dosimetry 122 396–400 [PubMed: 17251248]

Nakane Y and Sakamoto Y 2001 Measurement of absorbed dose distributions in a plastic phantom irradiated by 40-and 65-MeV quasi-monoenergetic neutrons Nuclear Instruments and Methods in Physics Research Section A: Accelerators, Spectrometers, Detectors and Associated Equipment 459 552–64

Paganetti H, Olko P, Kobus H, Becker R, Schmitz T, Waligorski MP, Filges D and Müller-Gärtner H-W 1997 Calculation of relative biological effectiveness for proton beams using biological weighting functions International Journal of Radiation Oncology• Biology• Physics 37 719–29

Pan CY, Huang YW, Cheng KH, Chao TC and Tung CJ 2015 Microdosimetry spectra and relative biological effectiveness of 15 and 30MeV proton beams Appl Radiat Isot 97 101–5 [PubMed: 25562679]

Paul H and Sánchez-Parcerisa D 2013 A critical overview of recent stopping power programs for positive ions in solid elements Nuclear Instruments and Methods in Physics Research Section B: Beam Interactions with Materials and Atoms 312 110–7

Perl J, Shin J, Schumann J, Faddegon B and Paganetti H 2012 TOPAS: an innovative proton Monte Carlo platform for research and clinical applications Med Phys 39 6818–37 [PubMed: 23127075]

Pihet P, Menzel H, Schmidt R, Beauduin M and Wambersie A 1990 Biological weighting function for RBE specification of neutron therapy beams. Intercomparison of 9 European centres Radiation Protection Dosimetry 31 437–42

Pshenichnov I, Botvina A, Mishustin I and Greiner W 2010 Nuclear fragmentation reactions in extended media studied with Geant4 toolkit Nuclear Instruments and Methods in Physics Research Section B: Beam Interactions with Materials and Atoms 268 604–15

Pshenichnov I, Larionov A, Mishustin I and Greiner W 2007 PET monitoring of cancer therapy with 3He and 12C beams: a study with the GEANT4 toolkit Physics in Medicine & Biology 52 7295 [PubMed: 18065840]

Pshenichnov I, Mishustin I and Greiner W 2006 Distributions of positron-emitting nuclei in proton and carbon-ion therapy studied with GEANT4 Physics in Medicine & Biology 51 6099 [PubMed: 17110773]

Pshenichnov I, Mishustin I and Greiner W 2008 Comparative study of depth–dose distributions for beams of light and heavy nuclei in tissue-like media Nuclear Instruments and Methods in Physics Research Section B: Beam Interactions with Materials and Atoms 266 1094–8

Rollet S, Colautti P, Grosswendt B, Moro D, Gargioni E, Conte V and DeNardo L 2010 Monte Carlo simulation of mini TEPC microdosimetric spectra: influence of low energy electrons Radiation Measurements 45 1330–3

Rossi HH 1979 The role of microdosimetry in radiobiology Radiation and environmental biophysics 17 29–40 [PubMed: 542603]

Schardt D, Elsässer T and Schulz-Ertner D 2010 Heavy-ion tumor therapy: Physical and radiobiological benefits Reviews of modern physics 82 383

Tran LT, Chartier L, Bolst D, Pogossov A, Guatelli S, Petasecca M, Lerch ML, Prokopovich DA, Reinhard MI and Clasie B 2017 Characterization of proton pencil beam scanning and passive beam using a high spatial resolution solid-state microdosimeter Medical physics 44 6085–95 [PubMed: 28887837]

Tran LT, Chartier L, Prokopovich DA, Reinhard MI, Petasecca M, Guatelli S, Lerch ML, Perevertaylo VL, Zaider M and Matsufuji N 2015 3D-Mesa “Bridge” Silicon Microdosimeter: Charge Collection Study and Application to RBE Studies in 12C Radiation Therapy IEEE Transactions on Nuclear Science 62 504–11

Underwood T, Sung W, McFadden C, McMahon S, Hall D, McNamara A, Paganetti H, Sawakuchi G and Schuemann J 2017 Comparing stochastic proton interactions simulated using TOPAS-nBio to

experimental data from fluorescent nuclear track detectors Physics in Medicine & Biology 62 3237 [PubMed: 28350546]

```
s:Sc/Scorer/Quantity    = "TsYScorer"
s:Sc/Scorer/Component   = "detector"
#
# Mandatory parameters
i:Sc/Scorer/GeometryNumber          = 0
d:Sc/Scorer/SensitiveVolumeRadius   = 0.45 mm   # radius of sensitive volume (except for silicon microdosimeter)
d:Sc/Scorer/TissueEquivalentRadius  = 0.5 um    # radius of equivalent size of tissue equivalent volume (to calculate mean chord length)
d:Sc/Scorer/TransX                  = 0 mm      # x position of sensitive volume from world center
d:Sc/Scorer/TransY                  = 0 mm      # y position of sensitive volume from world center
d:Sc/Scorer/TransZ                  = 0 mm      # y position of sensitive volume from world center
s:Sc/Scorer/OutputType              = "ROOT"    # OutputType must be ASCII, Binary or ROOT (unit: keV/um)
s:Sc/Scorer/IfOutputFileAlreadyExists = "Overwrite"
#
# Optional parameters
u:Sc/ Scorer /LinealEnergyUpperlimit          = 0.3       # in unit of keV/um
u:Sc/ Scorer /LinealEnergyLowerlimit          = 1000      # in unit of keV/um
b:Sc/Scorer/IncludeFrequencyMeanLinealEnergy  = "True"
b:Sc/Scorer/IncludeDoseMeanLinealEnergy       = "True"
b:Sc/Scorer/GetRBEWithBioWeightFunction       = "True"
b:Sc/Scorer/GetRBEWithMKModel                 = "True"
```

Figure 1.

An example of a TOPAS parameter file to invoke the lineal energy scorer and set necessary parameters.

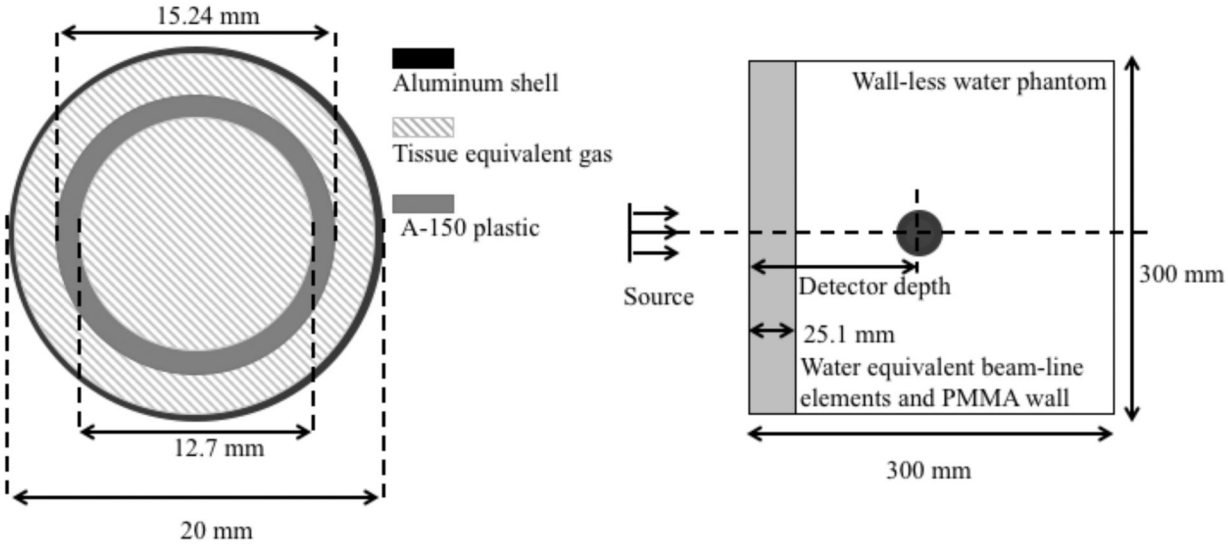

Figure 2.

Left: Simplified spherical TEPC structure used in the TOPAS simulation. The aluminum shell is 0.18 mm thick and has an outer diameter of 20 mm while the A-150 plastic sphere is 1.27 mm thick and has an internal diameter of 12.7 mm. Right: The geometry setup in the TOPAS simulation. The beam-line elements and PMMA wall of the water phantom are approximated as a 25.1 mm water slab in the simulation.

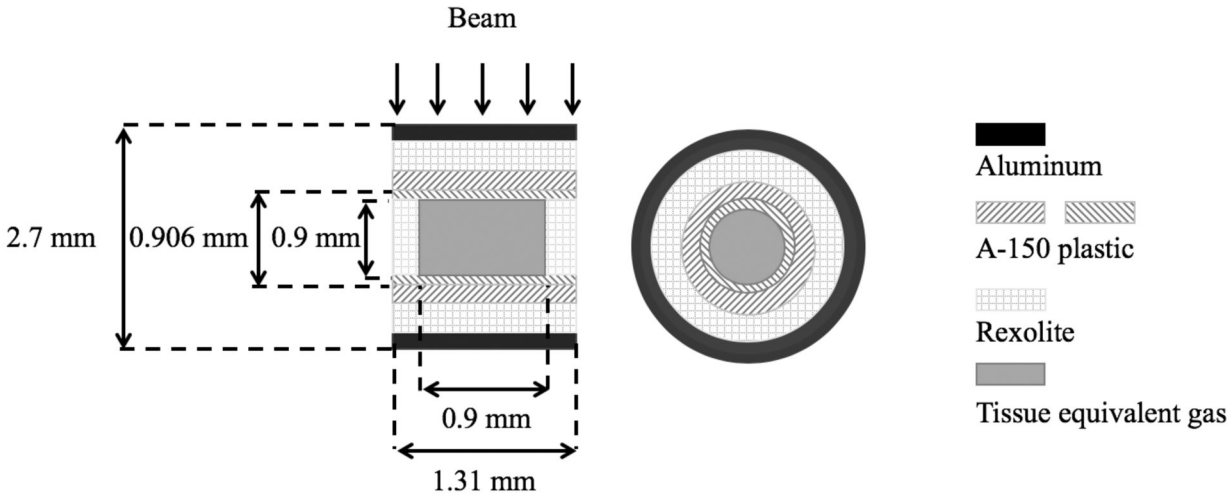

Figure 3.
The geometry of cylindrical mini-TEPC geometry in side (left) and front (right) view.

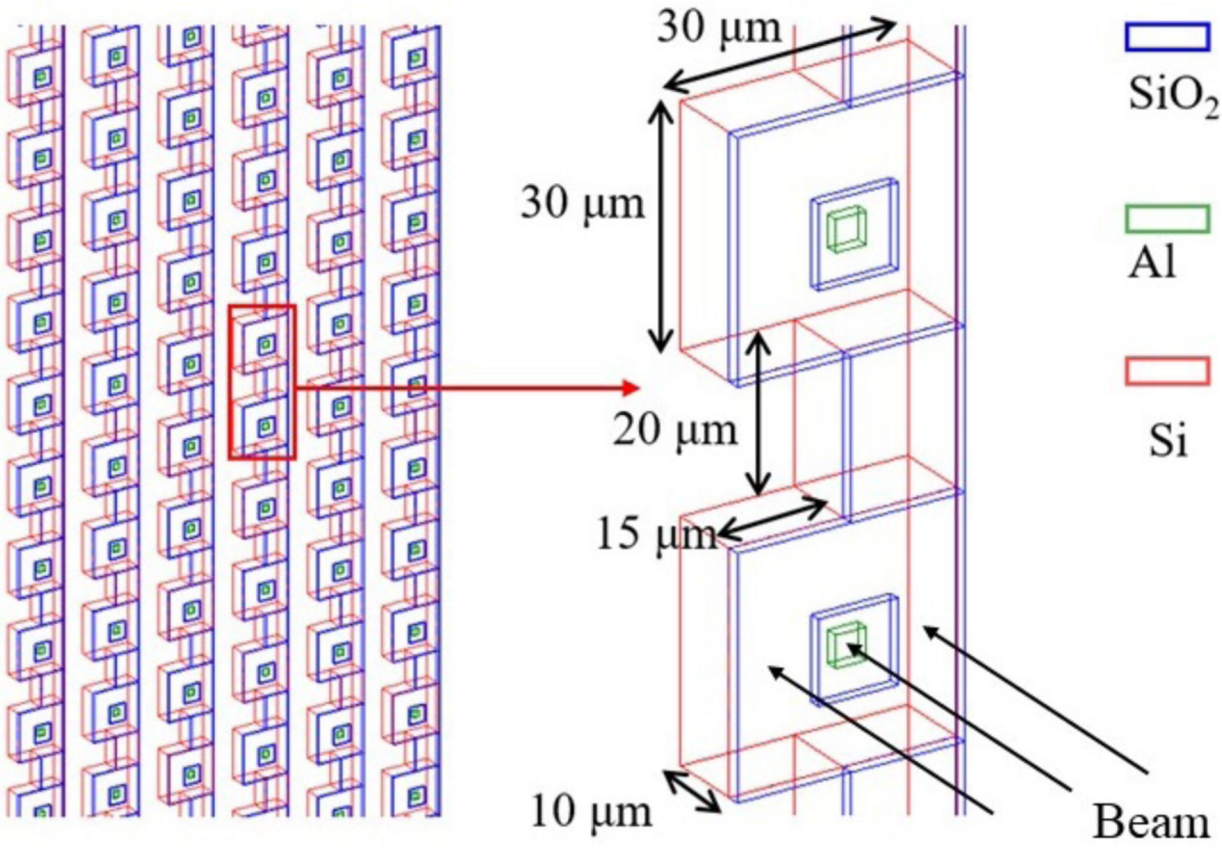

Figure 4.
The geometry of the SOI detector implemented as a TOPAS extension (TsSOIMicrodosimeter). The Si substrate and SiO_2 insulation layer are not shown in this visualization.

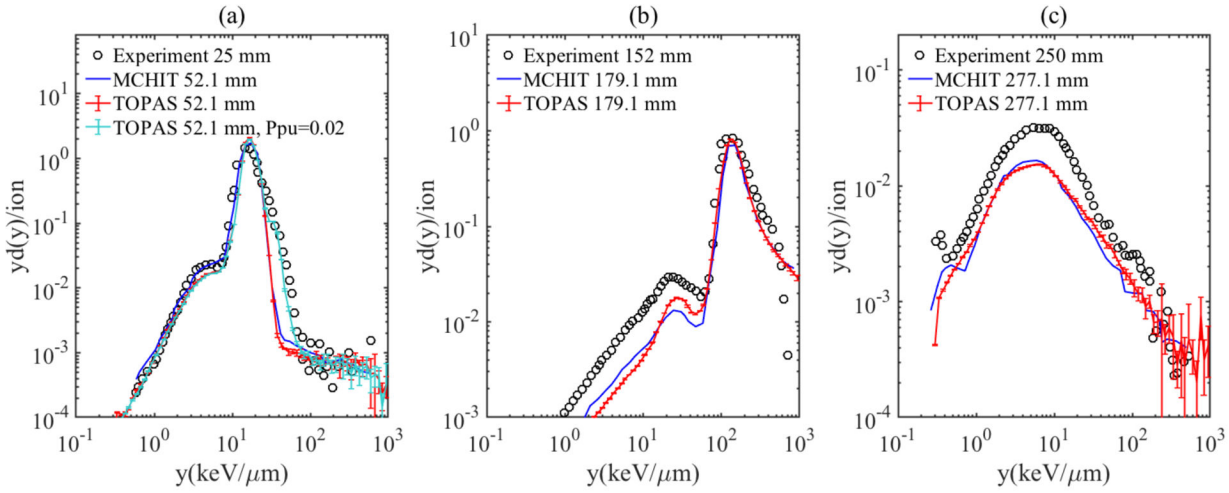

Figure 5.

Comparison of microdosimetric spectra of a 300 MeV/u carbon ion beam measured and simulated with MCHIT with G4BIC model and with TOPAS (a) at the plateau region (b) at the Bragg peak position and (c) at the tail region. The detector depth in wall-less water phantom in MCHIT and TOPAS simulations equals the detector depth in water phantom (25/152/250 mm) in experiment plus the equivalent water thickness in front of the phantom (25.1 mm) and the depth shift (2 mm). P_{pu} in panel (a) is the pile-up probability for each event. The error bars shown in the figure are the standard deviations, which were calculated with 1000 times of spectra update during the simulation, of each bin of the microdosimetric spectra.

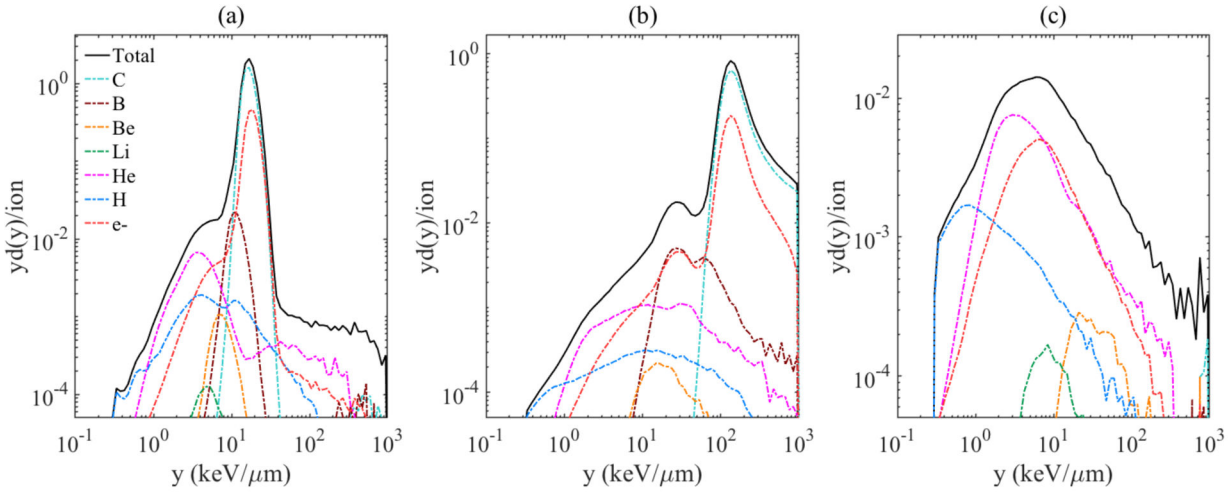

Figure 6.

Secondary particles contribution of a 300 MeV/u carbon ion beam obtained with TOPAS (a) at the plateau region (b) at the Bragg peak position and (c) at the tail region.

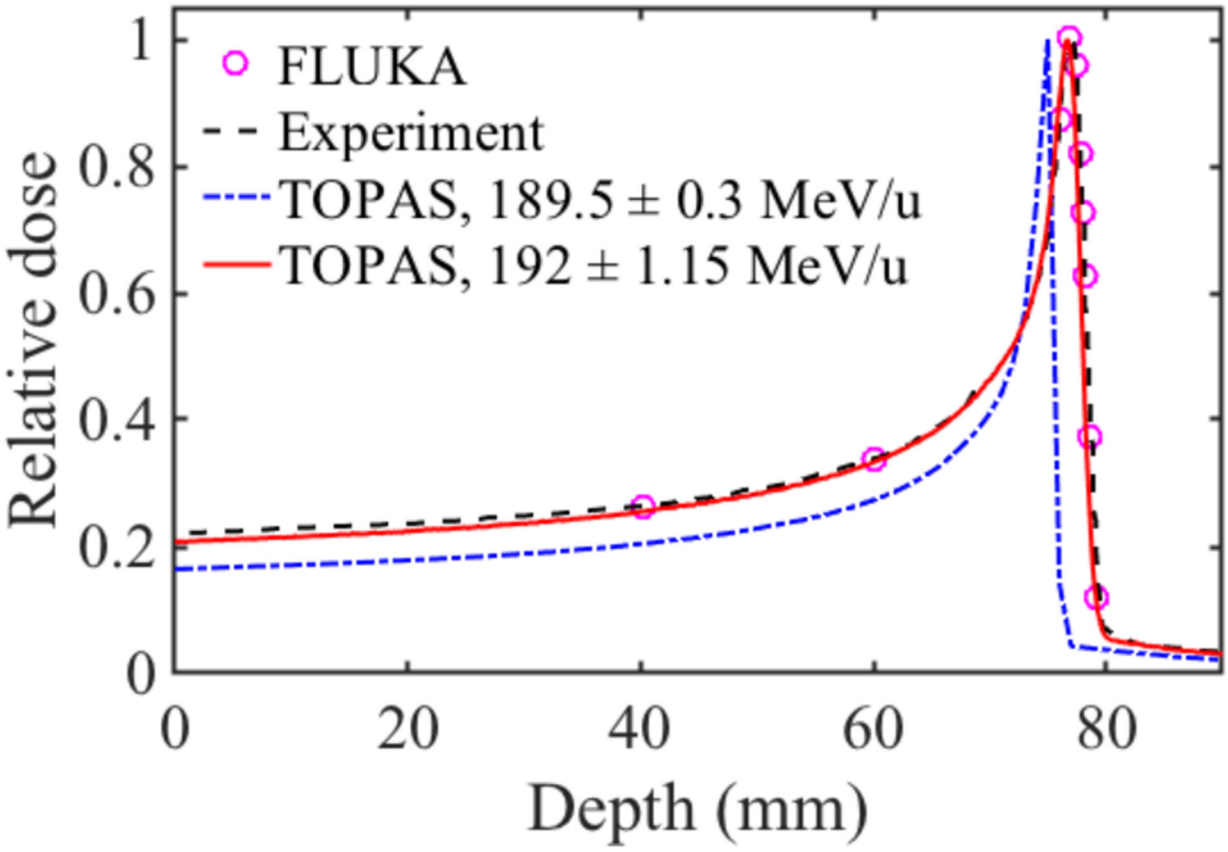

Figure 7.
Comparison of depth dose distributions obtained with FLUKA simulations, measured with a Markus chamber, and simulated with TOPAS.

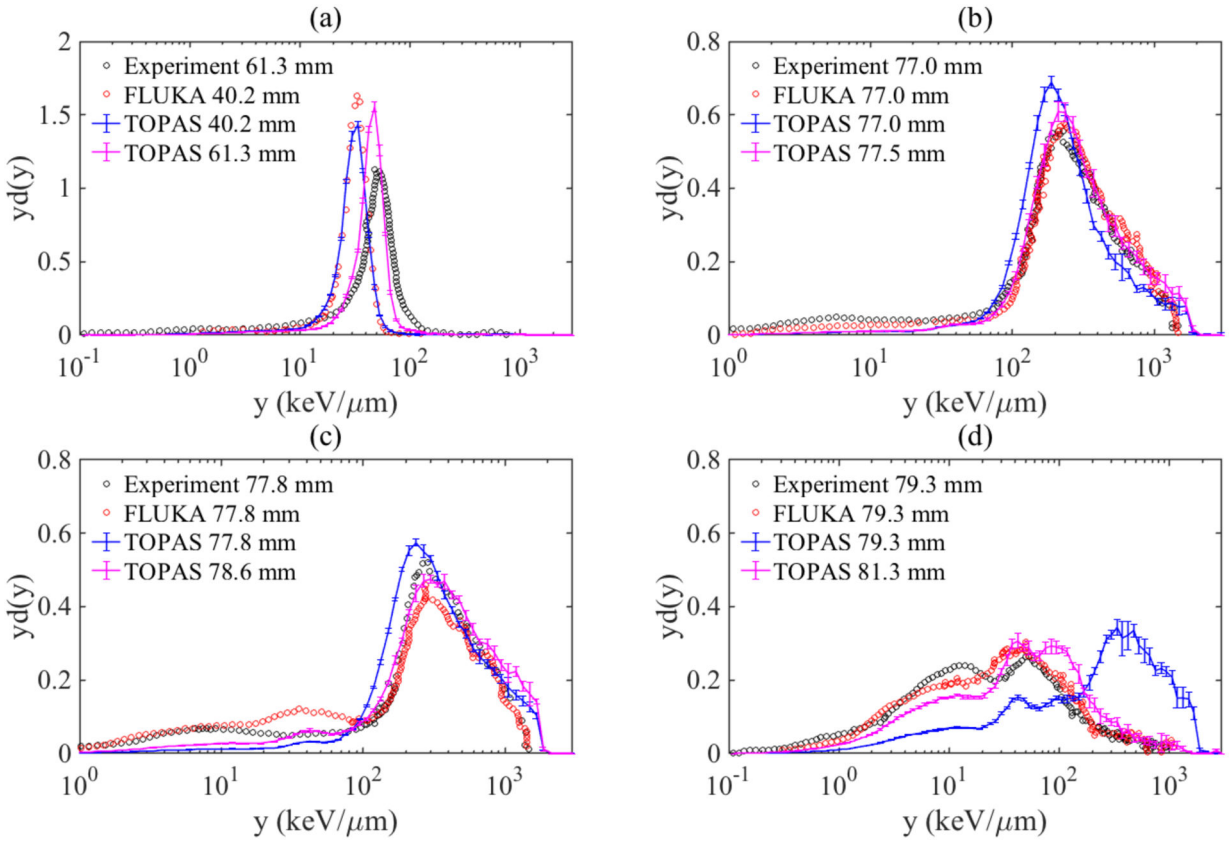

Figure 8.

Comparison of microdosimetric spectra obtained from experiment on carbon ion beam with an adjusted energy of 195.2 MeV/u, FLUKA, and TOPAS simulations. The comparison is performed (a) at two positions in the plateau region (40.2 and 61.2 mm), (b) at the Bragg peak (77.0 mm), (c) on the distal edge (77.8 mm) and (d) at the distal tail of the Bragg peak (79.3 mm). The error bars shown in the figure are the standard deviations, which were calculated with 1000 times of spectra update during the simulation, of each bin of the microdosimetric spectra.

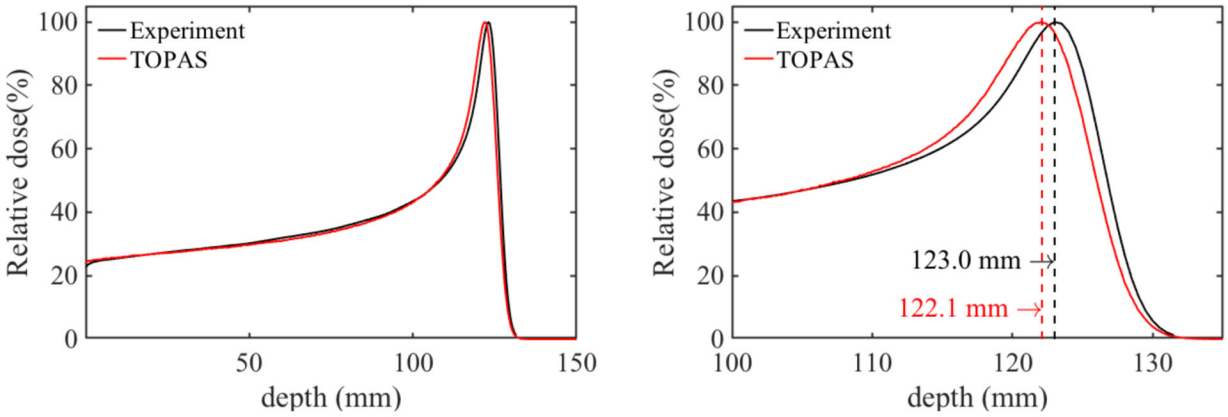

Figure 9.

Comparison of depth dose distributions of 131 MeV proton pencil beam scanning beam obtained experimentally and simulated with TOPAS along the whole proton range (left) and around the Bragg peak (right).

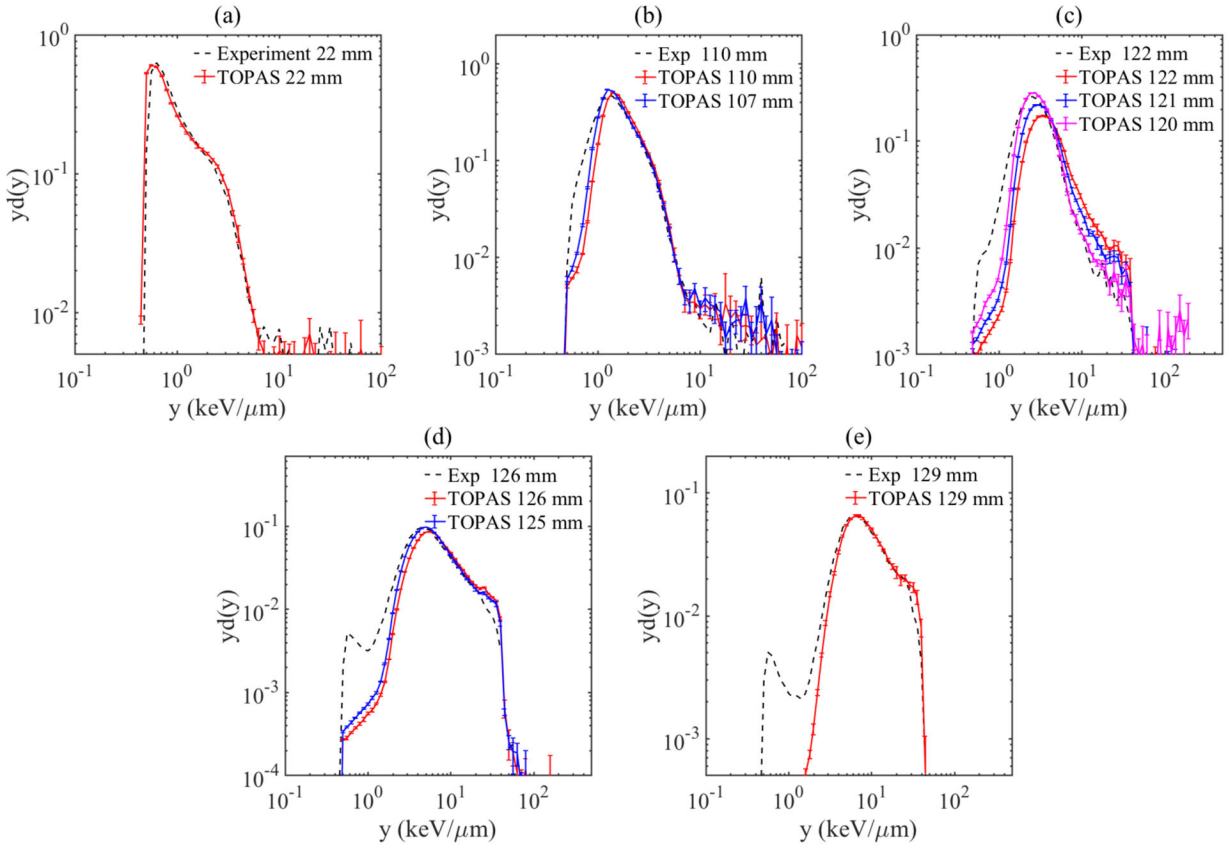

Figure 10.

Comparison of microdosimetric spectra obtained from experiment on a 131 MeV proton pencil beam scanning beam and simulated with TOPAS at various depths from the plateau region to the distal edge of the Bragg peak as indicated. The error bars shown in the figure are the standard deviations, which were calculated with 1000 times of spectra update during the simulation, of each bin of the microdosimetric spectra.

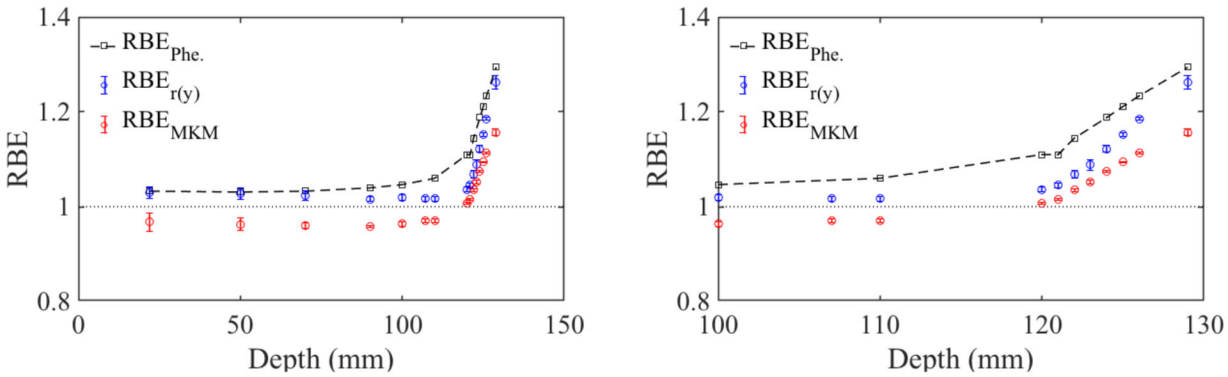

Figure 11.

RBE calculated with the phenomenological RBE model ($RBE_{phe.}$), biological weighting function approach ($RBE_{r(y)}$), and RBE_{10} calculated with the MK model (RBE_{MKM}) for 131 MeV proton pencil beam scanning beam showing the data along the whole proton range (left) and around the Bragg peak (right).

Table 1.

Input parameters of the lineal energy scorer

Mandatory parameters	**Type**	**Note**
GeometryNumber	integer	0 for the spherical TEPC, 1 for the cylindrical mini-TEPC and 2 for the silicon microdosimeter
TransX /TransY/ TransZ	double	X/Y/Z position of sensitive volume
SensitiveVolumeRadius	double	Radius of sensitive volume (except for silicon microdosimeter)
SensitiveVolumeHalfLength	double	Height of sensitive volume of cylindrical TEPC
TissueEquivalentRadius	double	Radius of tissue equivalent volume (applied for spherical and cylindrical TEPCs)
MeanPathLength	double	Mean path length of charged particles which cross the SV (applied for SOI microdosimeter)
Optional parameters	**Type**	**Note**
LinealEnergyUpperlimit	double	Upper threshold of lineal energy scorer
LinealEnergyLowerlimit	double	Lower threshold of lineal energy scorer
IncludeFrequencyMeanLinealEnergy	boolean	Whether to output frequency mean lineal energy, $\overline{y_F}$, default true
IncludeDoseMeanLinealEnergy	boolean	Whether to output dose mean lineal energy, $\overline{y_D}$, default true
GetContributionOfSecondaries	boolean	Whether to output the secondary particles contribution to the microdosimetric spectrum, default true
GetStatisticInformation	boolean	Whether to get statistic information, default true
SpectrumUpdateTimes	integer	How many times to update *f(y)* to calculate statistic information, default 1000
GetRBEWithBiologicalWeightFunction	boolean	Whether to calculate RBE with a weighting function, default false
GetRBEWithMKModel	boolean	Whether to calculate RBE with MK model, default false
MKModel_alpha0 *MKModel_beta* *MKModel_rho* *MKModel_rd* *MKModel_y0*	double	Parameters of the MK model in Eq.(6)–(7), default values used were 10% cell survival relative to 200 kVp X-rays for HSG cells, α_0= 0.13 Gy–1, β= 0.05 Gy-2, ρ= 1 g cm–3, rd= 0.42 μm, and y_0=150 keV/μm (Kase *et al.*, 2006; Kase *et al.*, 2013; Kase *et al.*, 2011)
BiologicalWeightFunctionDataFile	string	The name of a two-column text file, in which the first row lists the value of the lineal energy, the second row is the value of biological weighting function r(y)

Table 2.

Comparison of $\overline{y_F}$ and $\overline{y_D}$ calculated per energy deposition event at various positions inside the water phantom, and the corresponding probability P_{TEPC} to deposit energy in the TEPC per beam particle. Results from the custom-built TOPAS are based on Geant4 version 10.4.p2, from TOPAS 3.1.3 on Geant4 version 10.3.p2, and from MCHIT on Geant4 version 9.4.

		Custom TOPAS [a]	TOPAS 3.1.3[a]	MCHIT	Experiment[b]
$\overline{y_F}$ (keV/μm)	Plateau	1.50E+01 (1.04E-02)	1.54E+01 (8.40E-03)	1.48E+01	1.51E+01
	Peak	9.76E+01 (9.96E-02)	1.04E+02 (1.43E-01)	9.74E+01	7.87E+01
	Tail	3.22E+00 (6.40E-03)	3.26E+00 (1.32E-02)	2.89E+00	3.52E+00
$\overline{y_D}$ (keV/μm)	Plateau	1.74E+01 (3.66E-02)	1.74E+01 (5.25E-02)	1.69E+01	1.81E+01
	Peak	1.81E+02 (3.02E-01)	1.82E+02 (5.42E-01)	1.77E+02	1.70E+02
	Tail	1.54E+01 (5.53E-01)	2.10E+01 (1.35E+00)	1.33E+01	1.43E+01
P_{TEPC}	Plateau	9.91E-01 (8.43E-05)	9.93E-01 (6.08E-05)	9.87E-01	--
	Peak	6.53E-01 (6.29E-04)	6.54E-01 (7.53E-04)	6.44E-01	--
	Tail	4.30E-02 (1.54E-04)	2.30E-02 (1.29E-04)	5.10E-02	--

(a) The standard devotions are given in parentheses.

(b) The experimental $\overline{y_F}$ and $\overline{y_D}$ values were calculated from microdosimetric distributions by Burigo *et al* (Burigo *et al*., 2013).